Check for updates

High Power Laser Science and Engineering, (2026), Vol. 14, e100, 8 pages.
doi:10.1017/hpl.2026.10185

HIGH POWER LASER SCIENCE AND ENGINEERING

RESEARCH ARTICLE

Achieving high efficiency and enhanced beam quality in laser wakefield acceleration

Jia Wang[1,2], Ming Zeng[1], Dazhang Li[1], Wentao Wang[2], Song Li[2], Ke Feng[2], and Jie Gao[1]

[1]*Institute of High Energy Physics, Chinese Academy of Sciences, Beijing, China*

[2]*State Key Laboratory of Ultra-intense Laser Science and Technology, Shanghai Institute of Optics and Fine Mechanics (SIOM), Chinese Academy of Sciences, Shanghai, China*

(Received 6 May 2026 UTC; revised 30 June 2026 UTC; accepted 15 July 2026 UTC)

Abstract

Laser wakefield acceleration, characterized by the extremely high electric field gradient exceeding 100 GV/m, is regarded as a compact and cost-affordable technology for the next generation of particle colliders and light sources. However, it has always been a major challenge to effectively increase the energy transfer efficiency from the laser to the accelerated beam, while ensuring the beam quality remains suitable for practical applications. This study demonstrates two-step dechirping of a nanocoulomb-class accelerated electron beam using shorter laser pulses. The electron beams with an energy spread of 5% can be generated with the energy transfer efficiency of 10%–30% in a large parameter space. For example, an electron beam with an energy of 420 MeV, a charge of 5.5 nC and an energy spread of approximately 10% can be produced using an 8.3 J laser pulse with a duration of 7.2 fs.

Keywords: beam loading; beam quality; high efficiency; laser wakefield accelerator

1. Introduction

Laser wakefield accelerators (LWFAs)[1] provide accelerating fields for charged particles that are orders of magnitude higher than those in conventional radio-frequency (RF) accelerators, enabling electrons to attain giga-electronvolt energies within centimeter-scale distances[2,3]. This capability makes LWFAs a promising alternative for next generation particle colliders and compact radiation sources[4,5]. Over the past decades, significant progress has been achieved in improving electron beam quality[6,7]. Through techniques such as controlled injection and plasma shaping, for instance, stable beams with charges of approximately 10 pC and energy spread at a few per-mille level have been demonstrated[8]. However, the underlying physical mechanisms that enable such narrow energy spreads often inherently limit the energy transfer efficiency. In LWFAs, the energy transfer efficiency from the laser pulse to the high-quality electron beam typically lies between 0.1% and 1%[2,9–11]. This limitation arises from several physical constraints. The dependence of the wakefield structure on the laser energy implies that, even if the laser energy is depleted only by half, the laser might not be able to drive the wakefield to accelerate electrons[12], preventing the electrons from being stably accelerated. The fact that the laser group velocity is lower than the speed of the electron beams causes the particles to outrun the accelerating phase, thus limiting the beam energy[13,14]. Moreover, beam-loading effects can significantly reduce the accelerating gradient, particularly when accelerating high-charge beams[15]. Although the beam-loading effect reduces the accelerating gradient, it plays an important role in reducing the energy spread of high-charge beams[16].

Recent efforts have sought to overcome these limitations. A scheme combining a tri-plateau plasma channel[17,18] with a nonlinearly chirped laser was proposed to mitigate the laser distortion and beam dephasing, thereby enhancing transfer efficiency while using controlled dynamic beam-loading to reduce correlated energy spread[19]. The high energy transfer efficiencies have also been reported in the plasma telescope configuration[20,21] and the wakefield driven by a CO_2 laser[22]. The high efficiency LWFA has also been investigated in the pump-depletion dominated bubble regime[23,24] and in subcritical density plasma[25]. Despite these advances, achieving simultaneous improvements in both beam quality and energy transfer efficiency with a simple and controllable

Correspondence to: D. Li, Institute of High Energy Physics, Chinese Academy of Sciences, Beijing 100049, China. Email: lidz@ihep.ac.cn; W. Wang, Shanghai Institute of Optics and Fine Mechanics, Chinese Academy of Sciences, Shanghai 201800, China. Email: wwt1980@siom.ac.cn

© The Author(s), 2026. Published by Cambridge University Press in association with Chinese Laser Press. This is an Open Access article, distributed under the terms of the Creative Commons Attribution licence (https://creativecommons.org/licenses/by/4.0), which permits unrestricted re-use, distribution and reproduction, provided the original article is properly cited.

https://doi.org/10.1017/hpl.2026.10185 Published online by Cambridge University Press

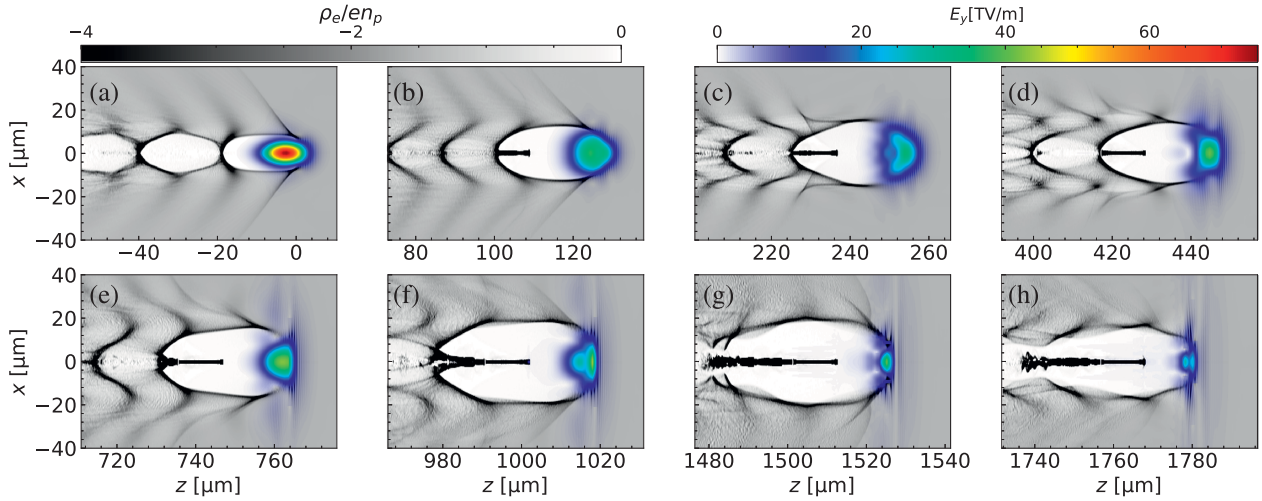


Figure 1. The snapshots of the plasma wakefield driven by a tightly focused laser pulse. (a)–(d) show the electron injection process driven by laser defocusing, where the bubble elongates and contracts due to the increasing laser radius after the focal point. (e)–(h) show the secondary injection process driven by pulse-front erosion, where the leading edge of the laser pulse becomes significantly eroded. The plasma has an unperturbed density of $n_p = 6 \times 10^{18}$ cm^{-3} and the laser has $a_0 = 15$, $w_0 = 6$ μm and $\tau_{FWHM} = 20$ fs. Here, ρ_e is the charge density of the plasma electrons and E_y is the envelope of the laser electric field.

setup remains a critical challenge, especially for applications such as particle colliders and X-ray free-electron lasers, which demand high charge and high beam quality.

In this paper, we propose and demonstrate an LWFA scheme that mitigates this challenge. Our approach uniquely leverages the laser defocusing injection mechanism[26] to enable efficient acceleration using an ultrashort (∼10 fs) drive laser. Within this injection scheme, the reduced pulse duration is naturally combined with a smaller focal spot, sustaining a high laser amplitude and a corresponding TV/m-scale wakefield[27] at multi-terawatt power levels. This strong wakefield suppresses beam loading for nC-scale charges, while the controlled pump depletion of the short driver induces a two-step dechirping dynamics that reduces correlated energy spread before the substantial beam dephasing occurs[7]. The optimal operating regime, with laser pulse duration as an essential control parameter, is efficiently identified through multi-objective Bayesian optimization (MOBO). We demonstrate, through particle-in-cell (PIC) simulations, the simultaneous generation of high-charge (∼nC) electron beams with approximately 20% energy transfer efficiency and narrow energy spread, representing a significant step toward practical, high-performance plasma accelerators.

2. Fundamental theory

In the injection mechanism facilitated by laser defocusing, the injection process itself imposes certain requirements on both the laser waist and the laser amplitude. Current theories[27,28] are not yet able to fully describe the relationship between the bubble length and the laser parameters, including the pulse duration, laser radius and intensity. However, it is clear that after the laser passes through its focal point, the attenuation of the laser intensity and the increase in the laser radius lengthen the nonlinear plasma wave[26,29]. This can explain the reduction in the phase velocity and the resulting injection dynamics.

Here, we perform one quasi-three-dimensional (3D) PIC simulation using the FBPIC code[30] with the Pseudo-Spectral Analytical Time Domain solver to show the laser defocusing injection, as depicted in Figure 1. The fully ionized plasma, with a plateau density of $n_p = 6 \times 10^{18}$ cm^{-3}, features an upramp defined by $n = n_p \exp\left(-z^2/\sigma_z^2\right)$ spanning from $z = -500$ μm to $z = 0$, where $\sigma_z = 200$ μm. The laser polarized in the y direction has the strength parameter of $a_0 = 15$, the laser waist of $w_0 = 6$ μm, the wavelength of $\lambda = 800$ nm and the focusing position of $z_f = 0$. The laser strength parameter a_0 is the peak amplitude of the normalized vector potential of the laser field $a = eA/m_e c^2$, with A being the amplitude of the vector potential. In addition, e is the elementary charge, m_e is the electron mass, c is the speed of light in vacuum and w_0 is the laser waist at the focal point in vacuum, defined as the radius at which the laser intensity drops to $1/e^2$ of its peak value. The full width at half maximum (FWHM) pulse duration τ_{FWHM} in this case is 20 fs, where τ_{FWHM} is the FWHM duration of the laser intensity. The simulations have the box size of $(100\ \mu m, 65\ \mu m)$ and grid numbers of $(256, 2048)$ in the r and z directions, respectively. The number of particles per cell along the (z, r, θ) directions is $(2, 2, 4)$, respectively. Two azimuthal modes are used. To reduce computational costs, ion motion is neglected in the simulations, and the reflective boundary condition is employed in the transverse direction. The snapshots in Figure 1 illustrate the evolution of the bubble and the electron injection process. The injection can be divided into two stages, corresponding to two distinct injection mechanisms. The first injection arises from the

https://doi.org/10.1017/hpl.2026.10185 Published online by Cambridge University Press

defocusing of the laser pulse (Figures 1(a)–1(d)), while the second injection originates from the carrier carrier-envelope phase (CEP) effect arising from sufficient pulse-front erosion[21,31–35].

Figure 2 shows the evolution of the laser radius w, laser intensity a and bubble length L_b. It can be seen that after the laser pulse passes through the focal point z_f, the laser radius w gradually increases and a decreases due to laser diffraction. This effectively promotes the longitudinal expansion of the bubble and reduces the phase velocity of the wakefield, leading to the rapid injection of an electron bunch. The transverse size of the bubble increases after the onset of injection, reaches a peak and subsequently decreases. This transverse contraction of the bubble causes the longitudinal size to shrink (see the orange curve in Figure 2(a)), thereby terminating the injection. The electron injection is confined to a narrow region between $z = 0$ and $z \sim 200$ μm, as indicated by the orange shaded area in Figure 2. After the laser defocusing injection ceased, the laser pulse continued to interact with the plasma. As this interaction proceeds, its pulse-front erosion effect became increasingly pronounced, inducing a fresh injection of electrons. This injection process lasted for approximately 1 mm, shown in the violet shaded area in Figure 2(a), and injected several nC of charge. Subsequently, as the laser pulse undergoes energy depletion, the bubble contracts. Meanwhile, the self-generated wakefield of the beam prevents the bubble from closing, thereby inhibiting further injection of background electrons (Figures 1(g) and 1(h)). To clarify the essence of the first injection process, a series of simulations with constant $a_0 w_0 = 15 \times 6$ μm are conducted to investigate the relationship of the bubble length L_b with the laser waist w_0 at the position before injection, that is, $z = z_f$. Note that a constant $a_0 w_0$ corresponds to a fixed laser power. As shown in Figure 2(c), this result confirms that the bubble elongation and contraction is caused by the laser defocusing, which promotes the reduction of the wakefield phase velocity, the injection of electrons and the subsequent termination of the injection. It should be noted that injection due to pulse-front erosion (in the violet region) has been discussed in another work[21,31–35], and is not considered in this work.

Previously, we obtained an empirical formula for the charge of the electron bunch injected via the laser defocusing injection, which is as follows[26]:

$$Q = C \times L_{inj} n_p a_0, \tag{1}$$

where $C = 1.19 \times 10^{-18}$ nC cm^2 is an empirical constant, L_{inj} is the injection length and n_p is the plasma density. The injection length is as follows:

$$L_{inj} = z_{Re} \sqrt{\exp(-1)\sqrt{2} a_0 / \left(\Gamma^2 k_p w_0\right) - 1}, \tag{2}$$

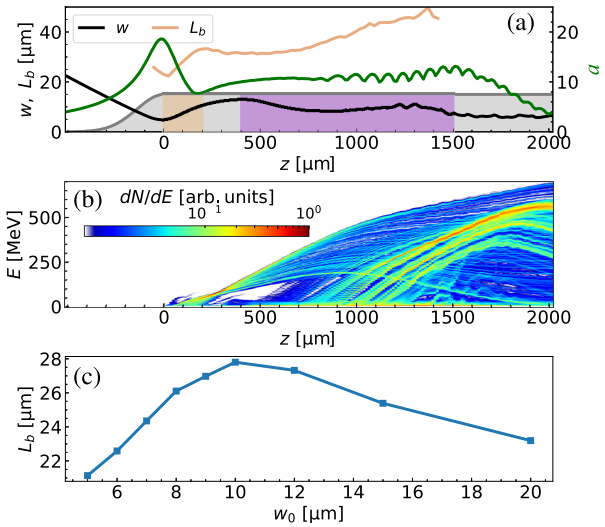


Figure 2. The evolution of the laser radius w, laser strength a and bubble length L_b (a) and the energy spectrum of the trapped electrons (b) with the laser position z. In (a), the gray region represents the density profile of the plasma, the orange region represents the zone dominated by injection driven by laser defocusing and the violet region corresponds to the zone dominated by a regular self-injection. (c) The relationship of the bubble length L_b with the laser waist radius w_0 at the position before injection is from a series of simulations with a constant $a_0 w_0 = 15 \times 6$ μm.

where $k_p = \omega_p / c$ and ω_p is the plasma frequency. The effective Rayleigh length within the first oscillation period of the laser pulse envelope $z_{Re} = \pi w_0^2 \Gamma^2 / \lambda$, where $\Gamma = w_{0e}/w_0$ and w_{0e} stands for the effective laser waist at the effective focal point for the laser in the plasma[26], and λ is the laser wavelength. We postulate the laser at the ending time of electron injection satisfies the matching condition $k_p w_m = 2\sqrt{a_m}$[13]. The laser radius is described as $w_m = \exp(-1/2)\left(2 w_0^2 a_0^2 / k_p^2\right)^{1/4}$ and a_m represents the matched laser strength for the matched state[26]. In addition, we assume the laser depletion length $L_{etch} = \omega^2 / \omega_p^2 c \tau_{FWHM}$ is related to the dephasing length $L_d = 2/3\omega^2/\omega_p^2 w_m$ by $L_{etch} = \alpha L_d$, where ω is the laser frequency. Here, $\alpha = 3 c \tau_{FWHM} / 2 w_m$ is a dimensionless coefficient.

By substituting the laser envelope $a = a_0 \exp\left(-t^2/\tau^2\right)$ into the one-dimensional (1D) nonlinear wakefield equation[27], we can obtain the normalized wakefield amplitude E_p. For the case where $0 < \alpha \leq 1$, the maximum energy gain can be expressed as follows:

$$\overline{E} = \frac{2}{3}(2-\alpha)\alpha E_p m_e c^2 \frac{\omega^2}{\omega_p^2}\sqrt{a_m}. \tag{3}$$

Subsequently the energy transfer efficiency for the electron beam with charge Q and energy $\overline{E}$ is given by the following:

$$\eta = \frac{Q}{e}\frac{\overline{E}}{E_L}, \tag{4}$$

https://doi.org/10.1017/hpl.2026.10185 Published online by Cambridge University Press

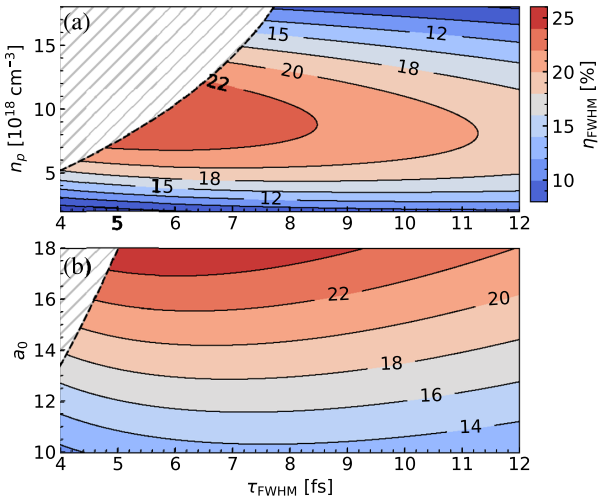


Figure 3. The distribution of the energy transfer efficiency according to the model, (a) with plasma density n_p and laser pulse duration τ_{FWHM}, while $w_0 = 6\,\mu m$ and $a_0 = 15$, (b) with laser strength parameter a_0 and laser pulse duration τ_{FWHM}, while $w_0 = 6\,\mu m$ and $n_p = 6 \times 10^{18}$ cm^{-3}. The practical parameters should be on the right-hand side of the dashed lines $\tau_{FWHM} = 2L_{inj}w_p^2/cw^2$, so that the laser pump-depletion length is sufficient for the acceleration.

where E_L is the laser energy and η is approximately related to η_{FWHM} as $\eta \sim 1.27 \times \eta_{FWHM}$, where η_{FWHM} corresponds to the energy transfer efficiency from the laser to the electrons with the charge of Q_{FWHM} in the FWHM range of the energy spectrum and $Q \sim 1.27 \times Q_{FWHM}$. We show the theoretical energy transfer efficiency according to this model in Figure 3. For the laser and plasma parameters of $a_0 = 15$, $w_0 = 6\,\mu m$ and $n_p = 6 \times 10^{18}$ cm^{-3}, Equation (4) indicates that the energy transfer efficiency attains its maximum value $\eta_{FWHM} \sim 21.5\%$ at a pulse duration of $\tau_{FWHM} \sim 6.3$ fs. This model predicts that if the pulse duration of the laser pulse can be compressed from 30 fs to around 10 fs, it will be beneficial for the energy transfer efficiency of the LWFA. Note that the laser pulse should have sufficient energy to drive the wakefield for removing the chirp of the injected beam, which means that L_{etch} should be sufficiently larger than L_{inj}. We assert the criteria to be $L_{etch} > 2L_{inj}$, or

$$\tau_{FWHM} > 2\frac{L_{inj}\omega_p^2}{c\omega^2}. \quad (5)$$

Thus, the practical parameters should be on the right-hand side of the curve $\tau_{FWHM} = 2L_{inj}\omega_p^2/c\omega^2$ in Figure 3.

3. Effect of pulse duration on beam quality

Here, we perform three additional PIC simulations to show the impact of the laser pulse duration on the beam quality and examine the model above, as depicted in Figure 4. In the plots, the black curves represent the energy spectrum of the electron beams dQ/dE, and the green curves represent longitudinal electric field E_z. The FWHM pulse durations τ_{FWHM} in the three cases are 5, 8 and 15 fs, respectively. The other laser and plasma parameters are the same as the case in Figure 1. For the case of $\tau_{FWHM} = 5$ fs, the laser pump-depletion length is too short, such that there is not enough length to remove the negative energy chirp of the electron beam. At $z \sim 530\,\mu m$ as shown in Figure 4(c), the beam has charge of $Q_{FWHM} \sim 0.76$ nC, the average energy of approximately 280 MeV, the FWHM energy spread of approximately 6.2% and the energy transfer efficiency of $\eta_{FWHM} \sim 15\%$, within FWHM range of the energy spectrum. For the case of $\tau_{FWHM} = 8$ fs, the chirp of the electron beam is removed twice at $z \sim 450\,\mu m$ and $z \sim 1060\,\mu m$ as shown in Figures 4(f) and 4(h), respectively. At $z \sim 1060\,\mu m$, the beam obtains the maximum energy of $\overline{E} \sim 372$ MeV, and has the charge of $Q_{FWHM} \sim 1.27$ nC, the energy spread of $\Delta E_{FWHM}/\overline{E} \sim 3.28\%$ and the energy transfer efficiency of $\eta_{FWHM} \sim 20\%$. Note that our model, that is, Equations (1), (3) and (4), predicts the beam parameters to be $\overline{E} = 360$ MeV, $Q_{FWHM} = 1.34$ nC and $\eta_{FWHM} = 21.1\%$, which are in good agreement with the simulation result as shown in Figure 5. For this moderate laser pump-depletion length, as the laser energy is gradually consumed in the plasma, the bubble shrinks and the beam-loading effect becomes more pronounced[15]. Consequently, the electric field E_z felt by the electron beam changes from having a positive longitudinal derivative ($dE_z/dz > 0$) to a negative one ($dE_z/dz < 0$). This in turn causes the longitudinal phase space (LPS) to rotate reversely, canceling the beam positive chirp. This two-step dechirping phenomenon caused by the laser depletion can also be observed in other injection schemes[7]. For the case of $\tau_{FWHM} = 15$ fs, the initial negative energy chirp of the beam is removed at $z \sim 290\,\mu m$ (Figure 4(j)) where the beams have the charge of $Q_{FWHM} \sim 0.84$ nC, the energy of approximately 109 MeV, the FWHM energy spread of approximately 5.06% and the energy transfer efficiency of $\eta_{FWHM} \sim 2.1\%$. However, the reversal of the phase rotation does not take place in this case, because the laser is still strong enough to drive a nonlinear wakefield with $dE_z/dz > 0$ even though the dephasing occurs, as the pump-depletion length is long in this case. Thus, the second removing of the energy chirp does not take place, and the beam quality is not as good as in the $\tau_{FWHM} = 8$ fs case. Here, we respectively refer to the dechirping mechanisms corresponding to long, moderate and short laser pump-depletion lengths (pulse duration) as the long-depletion regime, moderate-depletion regime and short-depletion regime.

4. Multi-objective Bayesian optimization

In order to optimize the parameters of beam energy spread and energy transfer efficiency that cannot be simultaneously considered in theory, and verify the strong dependence between beam quality and laser pulse duration, MOBO[36–38]

https://doi.org/10.1017/hpl.2026.10185 Published online by Cambridge University Press

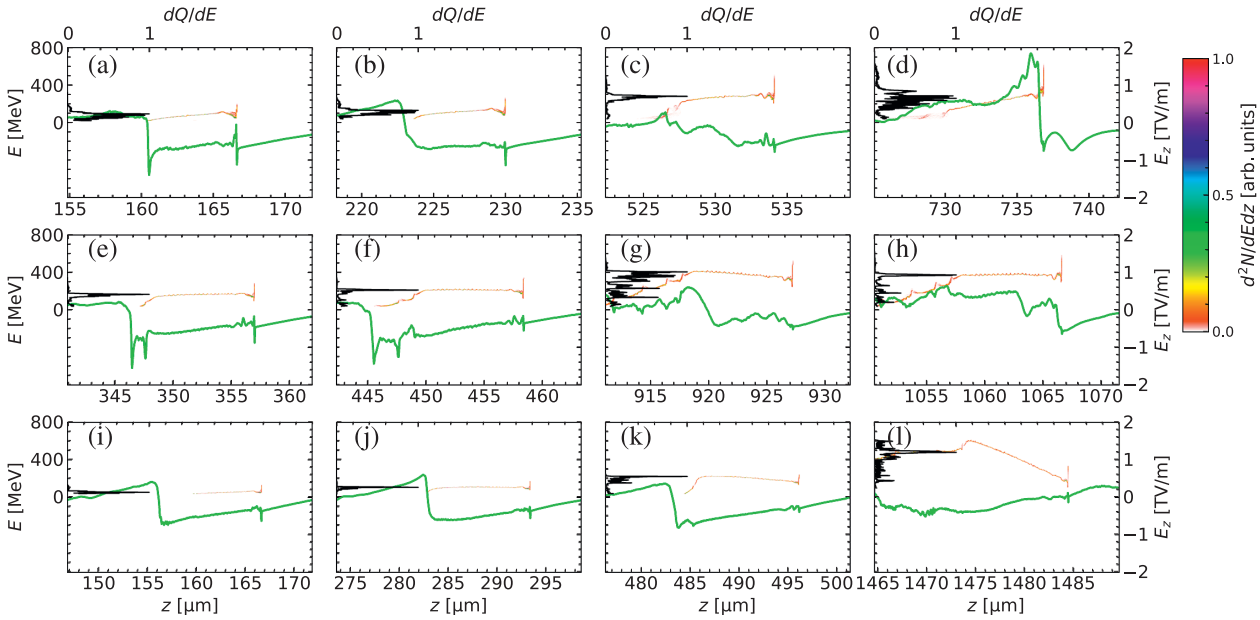


Figure 4. The phase-space distributions and the spectra dQ/dE (black curves) of the electron beam during the acceleration process for different laser duration cases. The distributions of the longitudinal electric field E_z, which are labeled on the right-hand axis, are also shown as the green curves. The laser durations are (a)–(d) $\tau_{\mathrm{FWHM}} = 5$ fs, (e)–(h) $\tau_{\mathrm{FWHM}} = 8$ fs and (i)–(l) $\tau_{\mathrm{FWHM}} = 15$ fs.

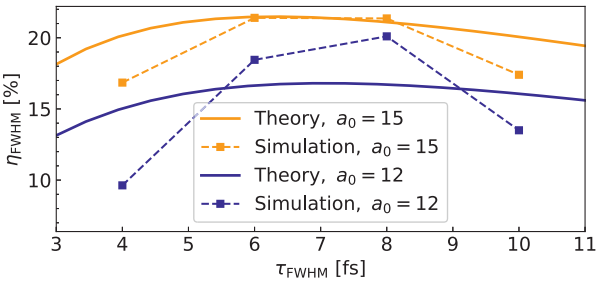


Figure 5. The comparison of energy transfer efficiency η_{FWHM} between the theory and simulations for different pulse durations τ_{FWHM}, while $w_0 = 6\ \mu$m and $n_{\mathrm{p}} = 6 \times 10^{18}\ \mathrm{cm}^{-3}$ are fixed.

is investigated for its ability to quickly evaluate and predict while relying on a very small amount of data by establishing surrogate models. MOBO can balance the objective functions by finding the Pareto front of the system. The cheap and fast Gaussian process (GP) is used as the surrogate model. The parallel Noisy Expected Hypervolume Improvement (qNEHVI)[39] is used as the acquisition function. During the optimization cycles, the plasma density n_{p}, laser strength parameter a_0, laser waist w_0 and laser pulse duration τ_{FWHM} are selected as the optimized input parameters. The plasma density is restricted to the range of $\left[4 \times 10^{18}\ \mathrm{cm}^{-3}, 8 \times 10^{18}\ \mathrm{cm}^{-3}\right]$. Considering the currently achievable laser power in experiment and the specific requirement of triggering this injection, the varying range of laser strength a_0 is between 8 and 20. In the laser defocusing injection scheme, the laser waist w_0 should be under 10 μm[26], because $w_0 = 10\ \mu$m is the transition from

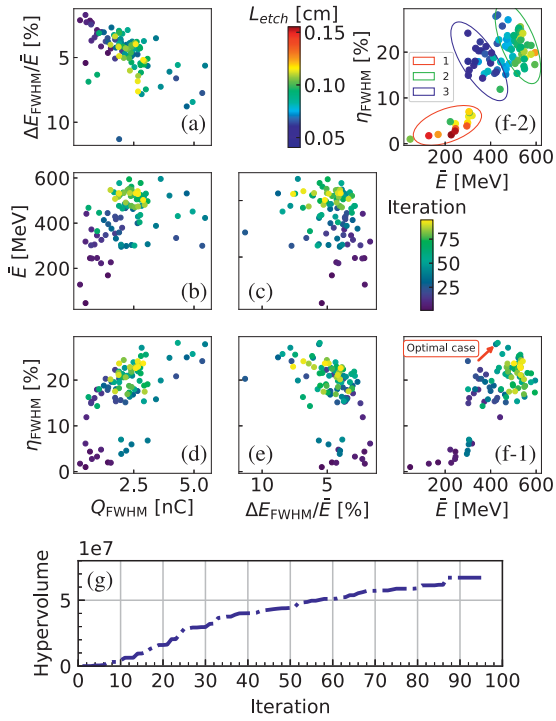


Figure 6. Diagram of the multi-objective Bayesian optimization. (a) The objective pairs of energy spread $\Delta E_{\mathrm{FWHM}}/\bar{E}$ versus charge Q_{FWHM}. (b) The beam energy $\bar{E}$ versus charge Q_{FWHM}. (c) The beam energy $\bar{E}$ versus energy spread $\Delta E_{\mathrm{FWHM}}/\bar{E}$. (d) The energy transfer efficiency η_{FWHM} versus charge Q_{FWHM}. (e) The energy transfer efficiency η_{FWHM} versus energy spread $\Delta E_{\mathrm{FWHM}}/\bar{E}$. (f-1) The energy transfer efficiency η_{FWHM} versus energy $\bar{E}$. In (f-2), three clusters of dots are categorized according to the associated laser depletion length L_{etch} and the legend numbers are indicative of the three types of dechirping mechanisms. (g) The evolution of the hypervolume over the iterations.

https://doi.org/10.1017/hpl.2026.10185 Published online by Cambridge University Press

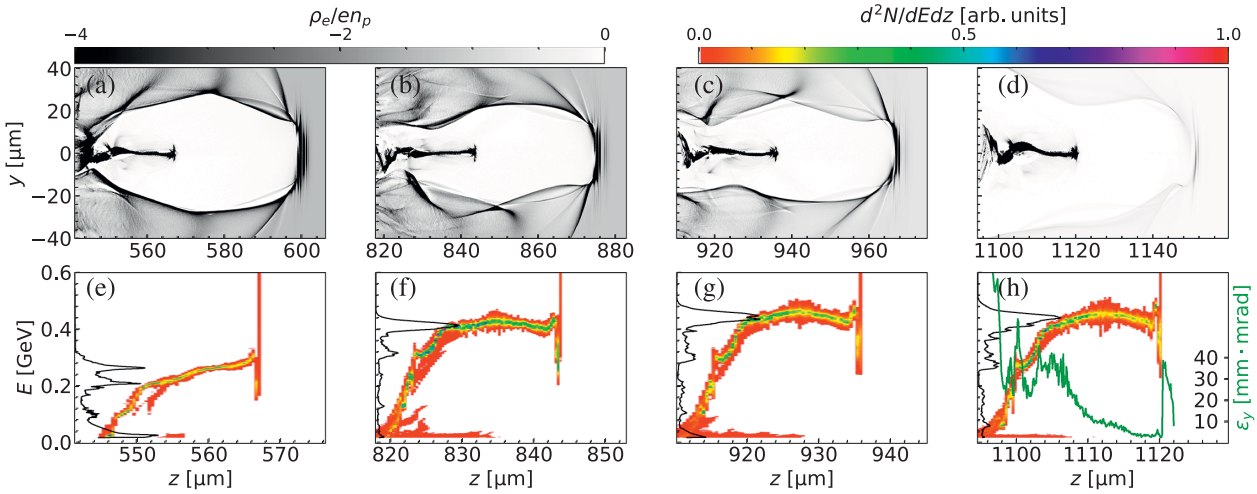


Figure 7. The snapshots of the plasma wakefield (a)–(d) and the corresponding distributions of the LPS (e)–(h) of the injected electron beam for the simulation with plasma density $n_p = 5.4 \times 10^{18}$ cm^{-3} and an 8.3 J laser at different positions. The black curves in (e)–(h) are the energy spectrum, and the green curve in (h) is the slice emittance. Because the head of the beam is positively chirped, this case belongs to the moderate-depletion regime.

the laser defocusing injection to general self-injection. We observed that the beam energy chirp cannot be removed if the laser waist is smaller than 4 μm, so the range of laser waist w_0 is set to [4 μm, 9 μm]. The range of the laser pulse duration τ_{FWHM} is from 5 to 20 fs, so that all three types of dechirping mechanisms are included in the optimization iteration. As the laser pulse interacts with the plasma over a longer distance before reaching its actual focal point, the effective Rayleigh length decreases. This, in turn, reduces the energy to which the beam can be accelerated. Therefore, for all simulations, the laser focus position is fixed at the entrance of the plasma density plateau.

We set four objective parameters for optimization: the charge Q_{FWHM}, the relative energy spread $\Delta E_{FWHM}/\overline{E}$, the average energy $\overline{E}$ and the corresponding energy transfer efficiency η_{FWHM}. The beam parameters at which the chirp of the beam is approximately removed are chosen as the training data. Upon executing nearly 100 iterations of the algorithm, the objective parameters are as depicted in Figure 6. Evidently, three separate Pareto fronts or clusters of points can be easily identified, which roughly correspond to the three types of dechirping mechanism described earlier. The behavior of the algorithm is observed to quickly deviate from the long-depletion regime and converge to the moderate-depletion regime. The electron beams generated in the moderate-depletion regime display higher energy and higher energy transfer efficiency. The physical trade-off between the charge and the energy spread broadens the spectrum of the beam as the charge is much higher (Figure 6(a)). Figure 6(g) shows the evolution of the hypervolume over the iterations. The hypervolume increases rapidly in the early stage and continues to grow throughout the optimization, indicating that the MOBO algorithm effectively explores the parameter space. Although full convergence has not been reached within 100 iterations, the hypervolume already shows a substantial improvement over the initial solutions, confirming the effectiveness of the MOBO approach in jointly optimizing the beam quality and the energy transfer efficiency.

5. Discussion

Generally, points lying on the Pareto front are considered optimal and are the desired targets of the optimization process. An example of such an optimal point is indicated by the red arrow in Figure 6(f-1), which corresponds to laser and plasma parameters of $a_0 = 20$, $w_0 = 9$ μm, $\tau_{FWHM} = 7.17$ fs and $n_p = 5.4 \times 10^{18}$ cm^{-3}. In the simulations and parameter optimization presented above, we did not account for the effect of the plasma exit (i.e., the down-ramp) on the beam quality, as it was unclear when the beam chirp would be eliminated. We now introduce the plasma exit into our simulations, whose density profile is symmetric to that at the plasma entrance. To maintain simulation accuracy, we accordingly increased the transverse resolution by increasing the cells from 256 to 1024 and setting the number of azimuthal modes to 4. Figures 7(a)–7(d) show the snapshots in the yz plane (i.e., the laser polarization plane). Transverse oscillations of the beam and the bubble are clearly observed, which arise from the single-cycle effect (CEP effect)[32] induced by the self-compression of the laser pulse. This effect also results in very large transverse momentum and emittance for the lately injected electrons (Figure 7(h)). The evolution of the beam parameters at the plasma exit reveals a marked increase in beam energy spread (Figure 8(b)). This deterioration is attributed to aggravated beam loading in the low-density region, where the trailing particles of the high-charge bunch

https://doi.org/10.1017/hpl.2026.10185 Published online by Cambridge University Press

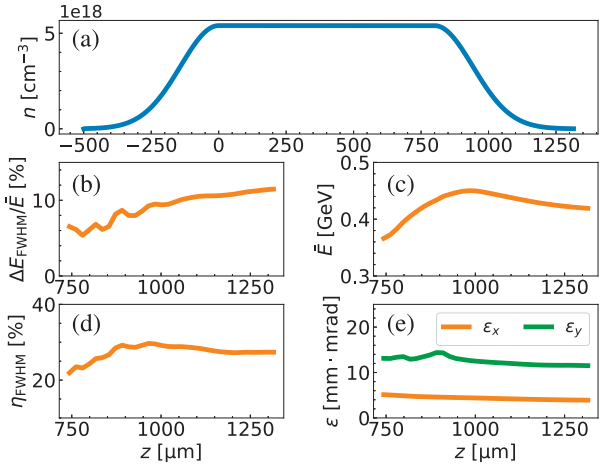


Figure 8. (a) The plasma density distribution for the simulation including the plasma down-ramp. The evolution of the energy spread $\Delta E_{\mathrm{FWHM}}/\overline{E}$ (b), energy $\overline{E}$ (c), energy transfer efficiency η_{FWHM} (d) and normalized emittance ε_x and ε_y (e) of the beam during passing through the plasma density down-ramp.

are strongly decelerated, thereby broadening the energy spectrum and compromising both the final beam energy and the transfer efficiency (Figures 8(c) and 8(d)). After passing through the plasma down-ramp, the electron beam has $Q_{\mathrm{FWHM}} = 5.4$ nC, energy spread of $\Delta E_{\mathrm{FWHM}}/\overline{E} \sim 11.45\%$, energy of $\overline{E} \sim 0.42$ GeV, energy transfer efficiency of $\eta_{\mathrm{FWHM}} \sim 27.33\%$ and normalized emittance of $\varepsilon_x \sim 3.9$ mm $\cdot$ mrad and $\varepsilon_y \sim 11.5$ mm $\cdot$ mrad. Note that we prioritized the optimization of beam charge to explore physics scenarios where high-charge beams are of particular interest, such as for radiation sources or beam-driven wakefield applications. While this comes at the cost of a reduced maximum energy, we believe this trade-off is worthwhile for applications that demand high charge[40,41] over ultra-high energy.

6. Conclusion

We have performed PIC simulations to show that LWFAs driven by moderately short laser pulse duration can have enhanced beam quality and energy transfer efficiency. By applying the laser defocusing injection scheme, a sub-petawatt laser pulse with a duration around 10 fs generates a nanocoulomb electron beam with an initially negative chirp, which is experiencing an automatic two-step dechirping process during the subsequent acceleration process. By employing MOBO, we show the generation of electron beams with high energy transfer efficiency of up to 28%, small energy spread of less than approximately 5%, energy of approximately 500 MeV and charge of approximately 5 nC using a 10 J laser. Our findings make a significant step toward compact accelerator-based applications.

Acknowledgements

This work was supported by the Strategic Priority Research Program of the Chinese Academy of Sciences (Grant Nos. XDB0530000 and XDB0890200), the National Natural Science Foundation of China (Grant Nos. 12475159, 12225411, 12388102, 12474349 and 12174410), the Key Research Program of Frontier Sciences of the Chinese Academy of Sciences (Grant No. QYZDJ-SSW-SLH004), the CAS Project for Young Scientists in Basic Research (Grant No. YSBR060), the CAS Youth Innovation Promotion Association (Grant No. 2022242) and the New Cornerstone Science Foundation through the Xplorer Prize.

References

1. T. Tajima and J. M. Dawson, Phys. Rev. Lett. **43**, 267 (1979).
2. A. J. Gonsalves, K. Nakamura, J. Daniels, C. Benedetti, C. Pieronek, T. C. H. de Raadt, S. Steinke, J. H. Bin, S. S. Bulanov, J. van Tilborg, C. G. R. Geddes, C. B. Schroeder, C. Tóth, E. Esarey, K. Swanson, L. Fan-Chiang, G. Bagdasarov, N. Bobrova, V. Gasilov, G. Korn, P. Sasorov, and W. P. Leemans, Phys. Rev. Lett. **122**, 084801 (2019).
3. B. Miao, J. E. Shrock, L. Feder, R. C. Hollinger, J. Morrison, R. Nedbailo, A. Picksley, H. Song, S. Wang, J. J. Rocca, and H. M. Milchberg, Phys. Rev. X **12**, 031038 (2022).
4. B. Foster, R. D'Arcy, and C. A. Lindstrøm, New J. Phys. **25**, 093037 (2023).
5. L. T. Mix, J. A. Maslow, M. A. Jaworski, and J. E. Coleman, Laser Part. Beams **42**, e1 (2024).
6. A. R. Maier, N. M. Delbos, T. Eichner, L. Hübner, S. Jalas, L. Jeppe, S. W. Jolly, M. Kirchen, V. Leroux, P. Messner, M. Schnepp, M. Trunk, P. A. Walker, C. Werle, and P. Winkler, Phys. Rev. X **10**, 031039 (2020).
7. J. Wang, M. Zeng, D. Li, X. Wang, W. Lu, and J. Gao, Matter Radiat. Extremes **7**, 054001 (2022).
8. L. T. Ke, K. Feng, W. T. Wang, Z. Y. Qin, C. H. Yu, Y. Wu, Y. Chen, R. Qi, Z. J. Zhang, Y. Xu, X. J. Yang, Y. X. Leng, J. S. Liu, R. X. Li, and Z. Z. Xu, Phys. Rev. Lett. **126**, 214801 (2021).
9. W. P. Leemans, B. Nagler, A. J. Gonsalves, C. Toth, K. Nakamura, C. G. R. Geddes, E. Esarey, C. B. Schroeder, and S. M. Hooker, Nat. Phys. **2**, 696 (2006).
10. W. P. Leemans, A. J. Gonsalves, H.-S. Mao, K. Nakamura, C. Benedetti, C. B. Schroeder, C. Tóth, J. Daniels, D. E. Mittelberger, S. S. Bulanov, J.-L. Vay, C. G. R. Geddes, and E. Esarey, Phys. Rev. Lett. **113**, 245002 (2014).
11. J. Götzfried, A. Döpp, M. F. Gilljohann, F. M. Foerster, H. Ding, S. Schindler, G. Schilling, A. Buck, L. Veisz, and S. Karsch, Phys. Rev. X **10**, 041015 (2020).
12. C. D. Decker, W. B. Mori, K. Tzeng, and T. Katsouleas, Phys. Plasmas **3**, 2047 (1996).
13. W. Lu, M. Tzoufras, C. Joshi, F. S. Tsung, W. B. Mori, J. Vieira, R. A. Fonseca, and L. O. Silva, Phys. Rev. ST Accel. Beams **10**, 061301 (2007).
14. J. P. Palastro, J. L. Shaw, P. Franke, D. Ramsey, T. T. Simpson, and D. H. Froula, Phys. Rev. Lett. **124**, 134802 (2020).
15. M. Tzoufras, W. Lu, F. S. Tsung, C. Huang, W. B. Mori, T. Katsouleas, J. Vieira, R. A. Fonseca, and L. O. Silva, Phys. Rev. Lett. **101**, 145002 (2008).
16. C. Rechatin, X. Davoine, A. Lifschitz, A. B. Ismail, J. Lim, E. Lefebvre, J. Faure, and V. Malka, Phys. Rev. Lett. **103**, 194804 (2009).

https://doi.org/10.1017/hpl.2026.10185 Published online by Cambridge University Press

17. B. M. Luther, Y. Wang, M. C. Marconi, J. L. A. Chilla, M. A. Larotonda, and J. J. Rocca, Phys. Rev. Lett. **92**, 235002 (2004).
18. S. Arjmand, R. Catalano, D. Oliva, A. Amato, C. Manna, A. D. Pappalardo, J. Suarez, and G. A. P. Cirrone, Laser Part. Beams **43**, e7 (2025).
19. S. Liu, F. Li, S. Zhou, J. Hua, W. B. Mori, C. Joshi, and W. Lu, Research **7**, 0396 (2024).
20. M. Zeng, A. M. de la Ossa, K. Poder, and J. Osterhoff, Phys. Plasmas **27**, 023109 (2020).
21. M. Zeng, Phys. Plasmas **31**, 080702 (2024).
22. E. Brunetti, R. N. Campbell, J. Lovell, and D. A. Jaroszynski, Sci. Rep. **12**, 6703 (2022).
23. V. Horný, P. G. Bleotu, D. Ursescu, V. Malka, and P. Tomassini, Phys. Rev. E **110**, 035202 (2024).
24. M. J. V. Streeter, Y. Ma, B. Kettle, S. J. D. Dann, E. G. Mayr, F. Albert, N. Bourgeois, S. Cipiccia, J. M. Cole, I. G. González, A. E. Hussein, D. A. Jaroszynski, K. Falk, K. Krushelnick, N. Lemos, N. C. Lopes, C. Lumsdon, O. Lundh, S. P. D. Mangles, Z. Najmudin, P. P. Rajeev, R. Sandberg, M. Shahzad, M. Smid, R. Spesyvtsev, D. R. Symes, G. Vieux, and A. G. R. Thomas, Phys. Rev. Accel. Beams **25**, 101302 (2022).
25. A. Ablimit, L. Q. Han, X. Y. Zhao, C. OuYang, H. Wen, and J. Q. Yu, Phys. Rev. Accel. Beams **29**, 013401 (2026).
26. J. Wang, M. Zeng, D. Li, X. Wang, and J. Gao, Phys. Rev. Accel. Beams **26**, 091303 (2023).
27. E. Esarey, C. B. Schroeder, and W. P. Leemans, Rev. Mod. Phys. **81**, 1229 (2009).
28. T. Matsuoka, C. McGuffey, P. G. Cummings, Y. Horovitz, F. D. lar, V. Chvykov, G. Kalintchenko, P. Rousseau, V. Yanovsky, S. S. Bulanov, A. G. R. Thomas, A. Maksimchuk, and K. Krushelnick, Phys. Rev. Lett. **105**, 034801 (2010).
29. H. Ding, A. Döpp, M. Gilljohann, J. Götzfried, S. Schindler, L. Wildgruber, G. Cheung, S. M. Hooker, and S. Karsch, Phys. Rev. E **101**, 023209 (2020).
30. R. Lehe, M. Kirchen, I. A. Andriyash, B. B. Godfrey, and J.-L. Vay, Comput. Phys. Commun. **203**, 66 (2016).
31. Y. F. Li, D. Z. Li, K. Huang, M. Z. Tao, M. H. Li, J. R. Zhao, Y. Ma, X. Guo, J. G. Wang, M. Chen, N. Hafz, J. Zhang, and L. M. Chen, Phys. Plasmas **24**, 023108 (2017).
32. E. N. Nerush and I. Y. Kostyukov, Phys. Rev. Lett. **103**, 035001 (2009).
33. J. Kim, T. Wang, V. Khudik, and G. Shvets, Phys. Rev. Lett. **127**, 164801 (2021).
34. Y. Ma, L. Chen, D. Li, W. Yan, K. Huang, M. Chen, Z. Sheng, K. Nakajima, T. Tajima, and J. Zhang, Sci. Rep. **6**, 30491 (2016).
35. W. Yan, L. Chen, D. Li, L. Zhang, N. A. M. Hafz, J. Dunn, Y. Ma, K. Huang, L. Su, M. Chen, Z. Sheng, and J. Zhang, Proc. Natl. Acad. Sci. U.S.A. **111**, 5825 (2014).
36. F. Irshad, S. Karsch, and A. Döpp, Phys. Rev. Res. **5**, 013063 (2023).
37. S. Jalas, M. Kirchen, C. Braun, T. Eichner, J. B. Gonzalez, L. Hübner, T. Hülsenbusch, P. Messner, G. Palmer, M. Schnepp, C. Werle, P. Winkler, W. P. Leemans, and A. R. Maier, Phys. Rev. Accel. Beams **26**, 071302 (2023).
38. M. Balandat, B. Karrer, D. R. Jiang, S. Daulton, B. Letham, A. G. Wilson, and E. Bakshy, Adv. Neural Inf. Proces. Syst. **33**, 21524 (2020).
39. S. Daulton, M. Balandat, and E. Bakshy, Adv. Neural Inf. Proces. Syst. **34**, 2187 (2021).
40. C. Y. Qin, X. S. Geng, H. Zhang, L. H. Yu, L. G. Zhang, Y. Z. Dai, J. Wang, B. W. Zhang, X. J. Guo, D. R. Xu, S. Xu, C. L. Ding, Y. Xu, Q. Liu, C. Wang, B. N. Shi, Z. X. Zhang, X. Y. Liu, Y. X. Leng, X. Y. Liang, B. F. Shen, L. L. Ji, and R. X. Li, Nat. Commun. **17**, 7540 (2026).
41. Z. Shi, W. Wang, X. Xie, J. He, H. Dong, X. Sun, H. Huang, B. Zhang, L. Yang, Z. Deng, F. Lu, W. Zhou, Y. Gu, Y. Leng, R. Li, and Z. Xu, Laser Part. Beams **43**, e2 (2025).

https://doi.org/10.1017/hpl.2026.10185 Published online by Cambridge University Press